Force Ripple Reduction of a Fractional Pole Pair Complementary Modularized Variable Reluctance Linear Machine for Long Stroke Application

Zhenghao Li, Shuangxia Niu, Xing Zhao and W. N. Fu

***Abstract*—Variable reluctance linear machine (VRLM), which takes advantages of magnet free, simple structure and low cost, is one of the emerging candidates for long stroke application. However, due to the abundant harmonics in the air gap, the conventional modular linear machine suffered from thrust ripple which leads to vibration and acoustic noise problem. The thrust force ripple in VRLM is mainly caused by higher-order harmonics in the induced voltage and detent force. To furtherly suppress the odd-order harmonics in the induced voltage and detent force, a fractional pole- pair unequal module arrangement (FP-UMA) design, in which the distances of adjacent modularized mover segments are not equal, is proposed to VRLM and collaborated with complementary structure in this paper. The key is that the modularized movers are artificially designed to be unequally distributed regarding to spatial distribution to eliminate the odd-order harmonics in the induced voltage along with the thrust ripples they caused based on the quantitative analysis on the thrust ripple components. It is revealed that, with the proposed FP-UMA design, the thrust ripple ratio of the machine has been effectively relieved from 4.6% to 2.2% under copper loss of 450W. Further, some design guidelines for the proposed machine, such as position offset of modularized mover $\Delta\lambda_{m2}$, DC loss ratio k_{dc} and slot pole combinations are discussed. In addition, the feasibility of the proposed design method is evaluated by finite element method as well as experiments.**

***Index Terms*—Force Ripple Reduction, Complementary Structure, Magnetless Linear Machine**

I. Introduction

Rail transmission system (RTS) is a type of high-capacity transmission system built for long-distance travel application. Eliminating the transmission device, linear machines (LM) have benefits of faster dynamic performance, lower noise, and higher efficiency comparing with its rotary counterparts and provide a better solution for RTS [1] [2].

For now, most of the LMs adopt permanent magnet (PM) material as excitation resource, which is known as PM linear synchronous machine (PMLSM). However, considering the high cost of permanent magnet (PM) material, PMLSM might not be a suitable actuator for long stroke applications. Therefore, magnet-less linear machines, such as linear induction machines (LIM) [3], switched reluctance linear machine (SRLM) [4] and Primary- excited linear machine (PELM) [5], are considered as potential candidates in direct-drive long stroke linear applications like RTS. LIMs, taking advantages of low-cost and simple secondary, have been researched for decades. However, experiencing eddy effect, LIMs suffer from low efficiencies and limited power density [3]. SRLM could achieve higher efficiencies and power density but result in complicated driving method and large thrust ripple [4].

PELM is an emerging linear machine in recent years, which features a compact short primary mover where both field excited source and armature winding are located [5]. Taking advantage of simple structure and less PM dosage, this machine is suitable for long stroke application. As a branch of PELM, DC- excited variable reluctance linear machine (DC-VRLM) [6][7], which is excited by DC current, and driven by the variable reluctance in the air gap, inherits the merits of robust and simple structure from PELM, and is totally PM free. However, due to its rich harmonics in the air gap, one of the most essential issues of this machine is its thrust ripple.

As a matter of fact, not only PELM, the thrust ripple in all kinds of linear machines has been investigated for decades. The state of art has been developed as follows. In early stage, the thrust- ripple suppression methods are proposed and applied in PMLSM [8]-[18]. Among these methods, skew method is the most common method, which have been widely adopted [8][9]. However, this method increases the manufacturing cost, and results in inevitable lower output thrust force. On the other hand, different kinds of auxiliary poles or teeth are added at the end of the linear machine to cancel the end effect [10]-[12]. However, this method aims to eliminate detent force and cannot fully suppress all the thrust ripple, whose effectiveness is limited. In addition, [12] proposed a complementary secondary for doubly salient linear machine (DSLM) to reduce the detent force and even- order harmonics in the induced voltage. [13] proposed a modulation method of the cogging force and end force to suppress the detent force of LM by adjusting the geometric dimensions of it. However, this method compromised the maximum output thrust. While some methods are focused on the improvements of the secondary parts, [14] and [15] discussed the method to utilize Halbach PM array to suppress thrust ripple by suppressing the higher- order harmonics in the flux densities. Apart from that, some direct thrust control strategy could be applied to the LM to reduce the thrust ripple of the linear machine [16]. However, it may cause the increase in computational complexity.

Modularized primary mover arrangement is an emerging method to relieve thrust ripple, which utilizes mutual restraint of the detent force for each module to eliminate detent force of the whole machine [17][18]. Meanwhile, reducing the coupling effect between different modules, it also enhances its fault

tolerance capability. This method is first applied to PMLSM in [17] and a consequence-pole PMLSM (CP-PMLSM) in [18], where the modules are evenly distributed. However, this method could only eliminate the fundamental and other order harmonics in the detent force except for third- and three-times' order harmonics. To further eliminate the remaining harmonics, fractional primary mover has been proposed in [19][20], and the higher order harmonics in the induced voltage and detent force have been perfectly eliminated. It is found that most of the existing work focused on the conventional PMLSM, which is not suitable for the long-stroke application. In [21], the arrangement of PM flux switching linear machine (PM-FSLM) is investigated, and it has been concluded that the 'AA-BB-CC' arrangements, where the two modules of the same phase are switched 180 degrees electrically, could achieve higher average thrust and lower thrust ripple. However, the principle of impact of modularized primary mover arrangement on the thrust ripple has not been fully investigated, and higher order harmonics in the induced voltage or detent force are not fully analyzed.

In this paper, a double- sided DC- excited modular variable reluctance linear machine (DS-DC-MVRLM) with complementary structure is proposed to suppress thrust ripple, and the arrangement of its modularized mover segments is investigated. Furthermore, a novel fractional pole- pair unequal module arrangement (FP- UMA) design has been proposed. The harmonics causing the thrust ripple are analyzed thoroughly and design guidelines on the unequal module arrangement and proposed machine are investigated to suppress the thrust ripples for the DC-MVRLM. The paper is organized as following: In Section II, the working principles of proposed DC-MVRLM along with its feasible module arrangements are discussed. In Section III, the sources of the thrust ripple are figured out, and method to suppress them is also discussed. In Section IV, the parametric analysis of this linear motor is carried out, and motors with feasible slot/ pole combination are compared. Section V specifically investigates the performance of the machine with/ without proposed FP-UMA design, including output thrust, efficiency, etc. The prototype of the machine is manufactured in Section VI. The finite element analysis (FEA) and experimental results are compared.

II. Machine Structure and Working Principle

A. Machine Configuration and Working Operation

Fig. 1(a) demonstrates the cross section of electromagnetic part of it. As shown in Fig. 1(a), the proposed DC-MVRLM employs double-side long stator with modular H-core mover design to accomplish a complementary structure. The primary part of the proposed machine consists of 6 modular segments. The magnetic-path connection between two neighbouring modules is cut off, and the secondary part of the machine adopts salient-pole teeth to construct a doubly salient structure. Comparing with conventional non-modularized design, flux barriers have been introduced between two adjacent phases to decouple the magnetic fields of them, and the mutual inductances between different phases of the linear motor are suppressed effectively. In this way, a fault occurring in some coils, would not affect the other coils. Thereby, the fault-tolerance capability of machines will be improved, and the reliability and stability of the whole system will be enhanced when it is applied to the RTS. Each module has four stator teeth wound with AC windings and DC windings wound on the yoke of each module. The secondary part has two segments located on both side of the mover, between which the screw electrical angle is set as π.

Adopting a double-sided structure, the 3D assembly structure of the prototype is illustrated as Fig.1 (b). The double sided long secondary part is laid along the track, between which the short modular primary mover part is installed. Different from PMLSM, the explosion of the cost of this transportation system along with the track length is avoided. Therefore, the proposed machine is especially suitable for long stroke application.

As shown in Fig.1(a), the working principle of MVRLM is provided as follows. When mover teeth align with the lower stator salient pole teeth, flux generated by the DC upper part would go through A11, Stator, and A12 to form the magnetic loop due to the minimum reluctance principle Vice versa, when the mover at position where mover teeth align with the upper stator, and the flux in A13 and A14 also reaches the top value in opposite direction. With the variable reluctance in the air gap, MVRLM realizes the conversion between the electrical and kinetic energy.

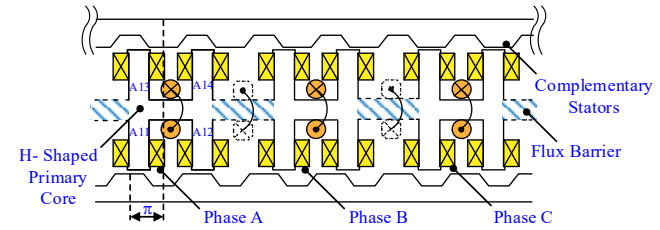

(a)

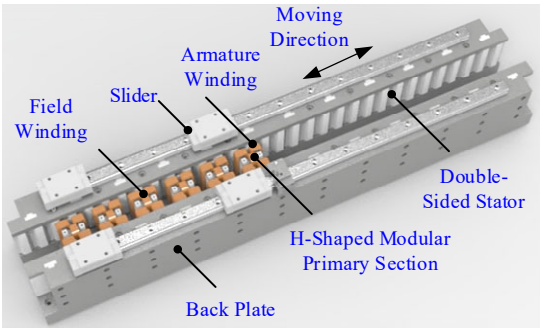

(b)

Fig. 1. Schematic of DC-MVRLM. *(a) Cross section. (b) 3D model.*

B. EMC Analysis of H-shaped Modular Core

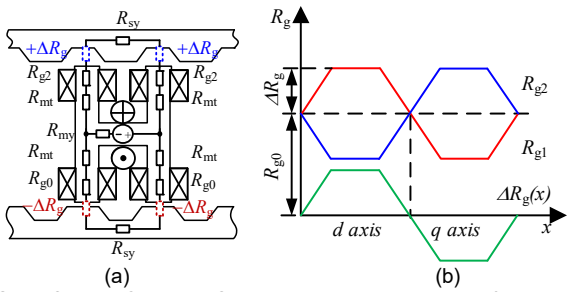

(a) (b)

Fig.2. Simplified EMC. *(a) EMC model. (b) Reluctance waveform.*

According to equivalent magnetic circuit (EMC) shown in Fig. 2(a), there are two symmetric magnetic return paths for the DC winding excitation ϕ_{dc}, where R_{sy} and R_{st} are the reluctance of stator yoke and stator teeth respectively, R_{my} is the mover yoke reluctance, R_{g1} and R_{g2} are air-gap reluctance at both sides, and the values of them are varied periodically according to relative mover's displacement. Fig.2 (b) illustrates the waveform of air-gap reluctance R_{g1} and R_{g2}. As shown in Fig.2

(b), the amplitudes of R_{g1} and R_{g2} are the same, but a change in the opposite direction. Therefore, the value of R_{g1} and R_{g2} can be expressed as (1) [22],

$$R_{g1,2} = R_{g0} \pm \Delta R_g(x) \tag{1}$$

where R_{g0} is the constant component of air gap reluctance $R_{g0} = \Lambda_{air}^{-1} w_{st}^{-1}(g + h_{st}/2)$, $\Delta R_g(x)$ is the variable component with respective to displacement of mover and $|\Delta R_g(x)| = \Lambda_{air}^{-1} w_{st}^{-1} h_{st}/2$, Λ_{air} is the permeability of air, w_{st} is the width of stator teeth, h_{st} is the height of stator teeth, and g is the length of air gap. The main flux ϕ_m can be solved using the cyclic current method, which is expressed as follows,

$$\begin{bmatrix} 2R_{mt}+2R_{g1}+R_{sy}+R_{my} & R_{my} \\ R_{my} & 2R_{mt}+2R_{g1}+R_{sy}+R_{my} \end{bmatrix} \begin{bmatrix} \phi_{m1} \\ \phi_{m2} \end{bmatrix} = \begin{bmatrix} F_{dc} \\ F_{dc} \end{bmatrix} \tag{2}$$

Solving (2), main flux linkages ϕ_m in both sides of airgap can be expressed with following equations,

$$\phi_{m1,2} = \frac{R_{my}\text{-}R_{2,1}}{R_{my}^2\text{-}R_2R_1} F_{dc} \tag{3}$$

where $R_1 = 2R_{mt}+2R_{g1}+R_{my}+R_{sy}$; $R_2 = 2R_{mt}+2R_{g2}+R_{my}+R_{sy}$.

To facilitate calculation, R_1 and R_2 are divided into constant and variable parts, rewritten as, $R_1 = R_0+\Delta R_g(x)$ and $R_2 = R_0-\Delta R_g(x)$ for parallel- complementary design, and $R_{1,2} = R_0+\Delta R_g(x)$ for non-complementary design. Substituting this to (3), the equation of main flux can be derived. Comparing the amplitude of main flux $|\phi_m|$ with/without parallel-complementary structure, denoted as ϕ_m/ ϕ'_m, can be defined as,

$$\delta = \frac{|\phi_m|}{|\phi'_m|} = \frac{(R_0 + R_{my})^2 - |\Delta R_g|^2}{R_0^2 - R_{my}^2 - |\Delta R_g|^2} \geq 1 \tag{4}$$

According to (4), it is found that the amplitude of main flux is determined by the reluctance of the mover yoke. Under no-load or light-load situation, when $R_{my} << R_0$, there is little difference of main flux linkage between DC-MVRLMs with/without complementary structure. However, as load increases, and the reluctance of mover yoke cannot be neglected, machine with complementary structure could obtain two times higher main flux linkage than machine without it.

On the other hand, Separating the flux linkages of module ϕ_m into upper ϕ_{l1} and lower part ϕ_{l2}, flux linkages, ϕ_m could be expressed as the sum of the two parts,

$$\begin{cases} \phi_m(t) = \phi_{l1}(t) + \phi_{l2}(t) \\ \phi_{l1}(t) = \phi_{l1(0)} + \sum\limits_{n1=1,2,3...} \phi_{l1(n)} \cos\left(n_1 \dfrac{2\pi}{\tau_s} v_m t \right) \\ \phi_{l2}(t) = -\left\{ \phi_{l2(0)} + \sum\limits_{n_1=1,2,3...} \phi_{l2(n1)} \cos\left[n_1 \dfrac{2\pi}{\tau_s} (v_m t + \tau_s) \right] \right\} \end{cases} \tag{5}$$

where n is the order of the flux linkages harmonics, v_m is the speed of the mover. Thanks to the complementary structure, the even- order component of the flux linkages in ϕ_{l1} and ϕ_{l2} have the same amplitude and phasor. The odd- order harmonics, however, have the same amplitude but reversed phasor. Therefore, the even order harmonics in ϕ_{m1} can be eliminated, when the two coils are connected in subtractive series. Therefore, the flux linkage, ϕ_m, only contains odd order harmonics and is expressed as following (6). In this way, the higher even-order harmonics in both flux linkages and induced voltage are eliminated, as well as the thrust ripple of the proposed motor.

$$\begin{aligned} \phi_m(t) &= \phi_{l1}(t) + \phi_{l2}(t) \\ &= \phi_{l1(0)} - \phi_{l2(0)} + \left\{ \begin{array}{l} \sum\limits_{n=1,2,3...} \phi_{l1(n)} \cos\left(n_1 \dfrac{2\pi}{\tau_s} v_m t \right) \\ - \sum\limits_{n=1,2,3...} \phi_{l2(n)} \cos\left[n_1 \dfrac{2\pi}{\tau_s} (v_m t + \tau_s) \right] \end{array} \right\} \\ &= 2 \sum_{n1=1,3,5...} \phi_{l1(n1)} \cos\left(n_1 \frac{2\pi}{\tau_s} v_m t \right) \end{aligned} \tag{6}$$

C. Modularized Mover Arrangements of DS- MVRLM

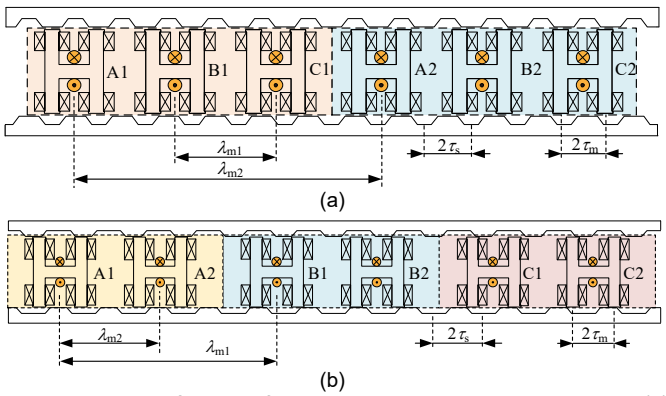

Fig.3.Parameter definitions of the two mover-segment arrangements. (a) "ABC-ABC" configuration. (b) "AABBCC" configuration.

Fig.3 defined the geometric dimensions on the arrangements of the linear machine. As denoted in Fig.3, the pole-pitch of the primary mover teeth is defined as τ_m, and the pole- pitch of secondary stator teeth is defined as τ_s. The pole-pitches of the modularized mover with adjacent phases and the same phases are defined as λ_{m1} and λ_{m2}, which could be obtained by the following equations,

(1) λ_{m1}, defined as the distance of the modules between two adjacent phases, could be calculated as,

$$\lambda_{m1} = (k_{m1} \pm \frac{1}{3}) \cdot \tau_s \text{ OR } \lambda_{m1} = (k_{m1} \pm \frac{1}{6}) \cdot \tau_s \tag{7}$$

(2) λ_{m2}, defined as the distance of modules with the same phase, could be calculated as follows,

$$\lambda_{m2} = k_{m2} \cdot \tau_s \text{ OR } \lambda_{m2} = (k_{m2} + \frac{1}{2}) \cdot \tau_s \tag{8}$$

where k_{m1} and k_{m2} are the positive integers. According to the different slot- pole combinations, which is defined by τ_m/ τ_s, the value of parameters k_{m1} and k_{m2} can be selected. In this paper, two kinds of arrangements of MVRLM are investigated, which is denoted as "ABC-ABC" and "AABBCC". Fig. 3 (a) and (b) illustrate two feasible arrangements of machine with each configuration, respectively. To be noticed, to make fair comparison, the τ_m of the machine is fixed to 32.5mm regardless of the arrangement of the module.

III. Force Ripple Components and Suppression

A. Thrust Ripple Analysis of Module Arrangement

According to [20], the thrust force of the machine composed of the electromagnetic force F_{em} and detent force F_{det}, the electromagnetic force can be calculated by following equation,

$$F_{total}(x) = F_{em}(x) + F_{det}(x) = F_{syn}(x) + F_{rl}(x) + F_{cog}(x) + F_{end}(x) \tag{9}$$

where F_{syn} is the DC-exited synchronous force of the motor, F_{rl} is the reluctance force of it, F_{cog} is the cogging force, and F_{end} is end force.

Furtherly, taken the positions of each module, shown in the Fig. 3, into consideration, the electromagnetic force of the whole motor, F_{em}, could be calculated as following,

$$F_{em}(x)=\sum_{i=1}^{3}F_{em\_m}^{(i)}\left[x+(i-1)\lambda_{m1}\right]+F_{em\_m}^{(i)}\left[x+(i-1)\lambda_{m1}+\lambda_{m2}\right] \quad (10)$$

where F_{em_m} is the electromagnetic force of each module, and i (i=1,2,3) is a positive integer.

Similarly, based on the positions of each module, the no-load detent force F_{det} of MVRLM can be expressed as,

$$F_{det}(x)=\sum_{i=1}^{3}F_{det\_m}^{(i)}\left[x+(i-1)\lambda_{m1}\right]+F_{det\_m}^{(i)}\left[x+(i-1)\lambda_{m1}+\lambda_{m2}\right] \quad (11)$$

where $F_{det\_m}(x)$ is the detent force of each module.

B. Fractional Pole-Pair Unequal Module Arrangement for Force Ripple Suppression

To overcome vibration and acoustic noise problem when the proposed machine is applied to RTS, the thrust force ripple of the machine should be further suppressed. Considering that modularized design is adopted in the proposed machine, the asymmetrical three-phase flux issue caused by end effect has been relieved, and higher-order harmonics in induced voltage plays main role in the thrust ripple in comparison [23]. In this part, to suppress the higher-order harmonics in induced voltage, and corresponding harmonics in the force, a novel fractional pole- pair unequal module arrangement (FP-UMA) design has been proposed. The harmonics causing the thrust ripple are analyzed thoroughly and design guidelines on the fractional pole-pair unequal module arrangement and proposed machine are investigated to suppress the thrust ripples for the MVRLM.

According to previous analysis and equation (6), the even-order harmonics in the flux linkage of one module has been completely cancelled. Therefore, the n_1th order induced voltage only contains odd-order harmonics, which can be expressed as,

$$\begin{bmatrix}E_{A1(n1)}(t)\\E_{B1(n1)}(t)\\E_{C1(n1)}(t)\end{bmatrix}=\frac{d}{dt}\begin{bmatrix}\phi_{A1(n1)}(t)\\\phi_{B1(n1)}(t)\\\phi_{C1(n1)}(t)\end{bmatrix}=\frac{d}{dt}\begin{bmatrix}\phi_{m(n1)}\cos\left[n_1\frac{2\pi}{\tau_s}(v_m t)\right]\\\phi_{m(n1)}\cos\left[n_1\frac{2\pi}{\tau_s}\left(v_m t+\frac{2}{3}\tau_s\right)\right]\\\phi_{m(n1)}\cos\left[n_1\frac{2\pi}{\tau_s}\left(v_m t-\frac{2}{3}\tau_s\right)\right]\end{bmatrix} \quad (12)$$

Furtherly, when three-phase sinusoidal armature current $i_{ABC}(t)$ is injected to the winding of the module, the electromagnetic force of three modules A1B1C1 generated by n_1th order induced voltage harmonic can be calculated as follows, when the saliency of the module is neglected [22],

$$\begin{cases}F_{em1}(x)=\dfrac{E_{A1(n1)}i_A+E_{B1(n1)}i_B+E_{C1(n1)}i_C}{v_m}=F_{em(n1)}\sin\left[\dfrac{2\pi}{\tau_s}(n_1\pm1)x\right]\\F_{em(n1)}=n_1\dfrac{2\pi}{\tau_s}\phi_{m(n1)}I_m\sin\left(\dfrac{n_1\pi}{2}\right)\left[2\cos\left(\dfrac{2(n_1\pm1)\pi}{3}\right)+1\right],x=v_m t\end{cases} \quad (13)$$

According to (13), the odd-order harmonics and harmonics which are not three multiples' order in F_{em1} have been eliminated. Therefore, only sixth and its multiples' harmonics are still remained in F_{em1}.

As shown in Fig. 3, the proposed MVRLM is composed of A1B1C1 and A2B2C2, and the n_1th components in the electromagnetic force of the whole machine is calculated as follows thereafter,

$$\begin{cases}F_{em(n1)}(x)=F_{em1(n1)}(x)+F_{em1(n1)}\left[x+\lambda_{m2}\right]\\=2F_{em1(n1)}\cos\left(\dfrac{\theta_{m2(n1)}}{2}\right)\left\{\sin\left[\dfrac{2\pi}{\tau_s}(n_1\pm1)x+\dfrac{\theta_{m2(n1)}}{2}\right]\right\}\\\theta_{m2(n1)}=2n_1\pi\dfrac{\lambda_{m2}}{\tau_s}.\end{cases} \quad (14)$$

where λ_{m2} is defined as distance of the modules with the same phase, whose corresponding n_1th angle difference is defined as $\theta_{m2(n1)}$.

To completely suppress the force ripple brought by sixth and higher order components, λ_{m2} can be modified to λ'_{m2} to make the second component $\cos\left(\frac{\theta_{m2(n1)}}{2}\right)$ in (14) equal to 0. In that case, $\theta_{m2(n1)}=(2k_1+1)\pi$, and the modified λ'_{m2} can be calculated with the following (15) thereafter,

$$\lambda'_{m2}=\frac{(2k_1+1)}{2n_1}\tau_s \quad (15)$$

where k_1 is an arbitrary natural number.

Fig. 4 illustrates the detent force of one module. As shown in Fig. 4, the detent force in the proposed machine could be divided into cogging force and end force. Since the mechanisms of the cogging force and end force are different, the components of them are also distinct.

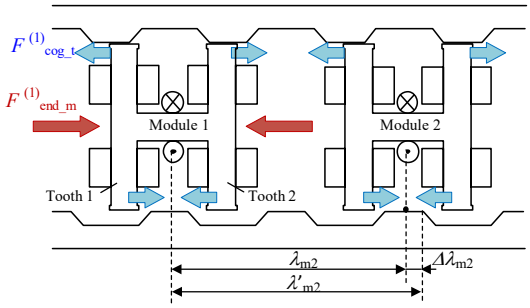

Fig.4.Detent force of the proposed MVRLM and modified λ_{m2}.

In terms of cogging force, taken module 1 in Fig. 4 as example, the cogging force of one tooth can be calculated as (16). Considering its double-sided complementary structure, the odd-order harmonics in the cogging force have been canceled.

$$F_{cog\_t}(x)=\sum_{n2=2,4,6...}F_{cog\_t(n2)}\cos\left[n_2\frac{2\pi}{\tau_s}x+\theta_{t0(n2)}\right] \quad (16)$$

where n_2 is the order of detent force harmonics, F_{cog_t1} is the amplitude of cogging force of Tooth 1, and θ_{t0} is the initial phase angle of Tooth 1.

As the displacement between Tooth 1 and Tooth 2 equals to τ_m, the corresponding angle difference of the cogging forces between two teeth is defined as $\theta_{t1(n2)}$, can be calculated as $2n_2\pi(\tau_m/\tau_s)$. Therefore, the n_2th components in the cogging force of Module i can be calculated as following (17),

$$\begin{cases} F_{\text{cog\_m}(n2)}^{(i)}(x) = F_{\text{cog\_t}(n2)}^{(i)}(x) + F_{\text{cog\_t}(n2)}^{(i)}(x+\tau_{\text{m}}) \\ = 2F_{\text{cog\_t}(n2)}\cos\left(\dfrac{\theta_{\text{t1}(n2)}}{2}\right)\cdot\cos\left[n_2\dfrac{2\pi}{\tau_{\text{s}}}x+\theta_{\text{t0}(n2)}+\dfrac{\theta_{\text{t1}(n2)}}{2}\right] \\ \text{where } \theta_{\text{t1}(n2)} = 2\pi\cdot n_2\dfrac{\tau_{\text{m}}}{\tau_{\text{s}}} \end{cases} \tag{17}$$

According to (17), the n_2th components of cogging force could be eliminated in the module component when $\theta_{\text{t1}(n2)} = (2k_2+1)\pi$, and k_2 is an arbitrary natural number.

As shown in Fig. 3, the angle difference of the modules between two adjacent phases is defined as $\theta_{\text{m1}(n2)}$, and the angle difference of the modules with the same phase is defined as $\theta_{\text{m2}(n2)}$. Taking the angles between different modules into consideration, the n_2th components in the cogging force of the whole machine is calculated as follows,

$$\begin{cases} F_{\text{cog}(n2)}(x) = \sum_{i=1}^{3} F_{\text{cog\_m}(n2)}^{(i)}\left[x+(i-1)\lambda_{\text{m1}}\right] + F_{\text{cog\_m}(n2)}^{(i)}\left[\left(x+\lambda_{\text{m2}}\right)+(i-1)\lambda_{\text{m1}}\right] \\ = 2F_{\text{cog\_m}(n2)}\cos\left(\dfrac{\theta_{\text{m2}(n2)}}{2}\right)\left[2\cos\theta_{\text{m1}(n2)}+1\right]\cos\left[n_2\dfrac{2\pi}{\tau_{\text{s}}}x+\theta_{\text{m1}(n2)}+\dfrac{\theta_{\text{m2}(n2)}}{2}\right] \\ \text{where } F_{\text{cog\_m}(n2)} = 2F_{\text{cog\_t}(n2)}\cos\left(\dfrac{\theta_{\text{t1}(n2)}}{2}\right),\ \theta_{\text{m1}(n2)} = 2n_2\pi\dfrac{\lambda_{\text{m1}}}{\tau_{\text{s}}},\ \theta_{\text{m2}(n2)} = 2n_2\pi\dfrac{\lambda_{\text{m2}}}{\tau_{\text{s}}}. \end{cases} \tag{18}$$

Substituting (7) into (19), $\theta_{\text{m1}(n2)} = \pm n_2\dfrac{\pi}{3}$, and the third component in (19), $2cos\left(\theta_{\text{m2}(n2)}\right)+1$, equals to 0, when n_2 is not the third and its multiples' harmonics.

As the odd-order harmonics in the cogging force have been canceled, only sixth and its multiples' harmonics are remained in the cogging force of MVRLM based on the calculation results in (18), (21) and (22), and other harmonics have been eliminated in theory. To completely suppress sixth and its multiples' harmonics in the cogging force, λ_{m2} could be modified to make the second component $\cos\left(\frac{\theta_{\text{m2}(n2)}}{2}\right)$ in (19) equal to 0. In that case, modified λ'_{m2} is redesigned following equation (19),

$$\lambda'_{\text{m2}} = \frac{(2k_2+1)}{2n_2}\tau_{\text{s}} \tag{19}$$

where k_2 is an arbitrary natural number.

The end force owing to the discontinuous modular primary core also causes thrust fluctuation. For the proposed modular machine, as shown in Fig. 4, there are two end forces for each module, and the end force for ith module, $F_{\text{end\_m}}^{(i)}$, can be calculated by combining those two end forces together. (20) calculated the n_3th order harmonics for $F_{\text{end\_m}}^{(i)}$,

$$\begin{cases} F_{\text{end\_m}(n3)}^{(i)}(x) = F_{\text{end\_ml}(n3)}\cos\left[n_3\dfrac{2\pi}{\tau_{\text{s}}}x+\theta_{\text{end0}(n3)}\right] \\ +F_{\text{end\_ml}(n3)}\cos\left[n_3\dfrac{2\pi}{\tau_{\text{s}}}\left(x+2\tau_{\text{m}}\right)+\theta_{\text{end0}(n3)}\right] \\ = 2F_{\text{end\_ml}(n3)}\cos\left(\dfrac{\theta_{\text{endl}(n3)}}{2}\right)\cdot\cos\left[n_3\dfrac{2\pi}{\tau_{\text{s}}}x+\theta_{\text{end0}(n3)}+\dfrac{\theta_{\text{endl}(n3)}}{2}\right] \\ \text{where } \theta_{\text{endl}(n3)} = 2\pi\cdot n_3\dfrac{2\tau_{\text{m}}}{\tau_{\text{s}}}. \end{cases} \tag{20}$$

Similarly, taken module arrangement into consideration, the end force of the whole motor can be calculated with the same method discussed in the cogging force,

$$\begin{cases} F_{\text{end}(n3)} = 2F_{\text{end\_m}(n3)}\cos\left(\dfrac{\theta_{\text{m2}(n3)}}{2}\right)\left[2\cos\theta_{\text{ml}(n3)}+1\right]\cos\left[n_3\dfrac{2\pi}{\tau_{\text{s}}}x+\theta_{\text{ml}(n3)}+\dfrac{\theta_{\text{m2}(n3)}}{2}\right] \\ \text{where } F_{\text{end\_m}(n2)} = 2F_{\text{end\_ml}}\cos\left(\dfrac{\theta_{\text{endl}(n3)}}{2}\right),\ \theta_{\text{ml}(n3)} = 2n_3\pi\dfrac{\lambda_{\text{ml}}}{\tau_{\text{s}}},\ \theta_{\text{m2}(n2)} = 2n_3\pi\dfrac{\lambda_{\text{m2}}}{\tau_{\text{s}}} \end{cases} \tag{21}$$

In the same way, λ_{m2} could be modified to make the second component $\cos\left(\frac{\theta_{\text{m2}(n3)}}{2}\right)$ in (22) equal to 0. Therefore, the modified λ'_{m2} is recalculated as equation (22),

$$\lambda'_{\text{m2}} = \frac{(2k_3+1)}{2n_3}\tau_{\text{s}} \tag{22}$$

Thereafter, according to (15), (19) and (22), modified λ'_{m2} is not integer multiple to stator pole-pitch τ_{s} to achieve lower force ripple of the machine comparing with conventional λ_{m2}. Therefore, the fractional pole-pair unequal module arrangement (FP-UMA) should be applied to the proposed machine to suppress sixth and higher order harmonics.

TABLE I FRACTIONAL POLE-PAIR UNEQUAL MODULE ARRANGEMENT

Force Component	Modified λ'_{m2}	Harmonics order	$\Delta\theta_{\text{c}}$(deg)
F_{em}	$\dfrac{(2k_1+1)}{n_1}\tau_{\text{s}}$	n_1=*5, 7, 6n ± 1…*	36
F_{cog}	$\dfrac{(2k_2+1)}{n_2}\tau_{\text{s}}$	n_2=*6, 12, 6n…*	30
F_{end}	$\dfrac{(2k_3+1)}{2n_3}\tau_{\text{s}}$	n_3=*6, 12, 6n…*	15

In specific, TABLE I summarizes remaining order harmonics of each force components and the recommended modified λ'_{m2} based on the analysis above under different module arrangement. However, it should be noted that some force components cannot be suppressed simultaneously, the tradeoff should be considered to select a proper λ'_{m2} thereafter.

C. Case Study

The dimension parameters of the machine are denoted in Fig. 5(a), where basic parameters for the proposed. In addition, the definition of the distance between modules of the same phase λ_{m2}, the definition of the distance between modules of the different phase λ_{m1} and the offset of modified mover pole- pitch $\Delta\lambda_{\text{m2}}$ are illustrated in Fig. 5(b).

Table II lists some key parameters of modular linear machine with $\tau_{\text{m}}/\tau_{\text{s}}$=10/12 in this case. To make a fair comparison and keep the total length of the mover within 400mm [22], the module pole pitch τ_{m} is designed as 32.5mm, the stator pole-pitch τ_{s} is fixed to 39mm thereafter. Meanwhile, to limit the total length of the linear motor and guarantee enough space to house winding, the distances between modules of the different (same) phase $\lambda_{\text{m1(2)}}$ should satisfy the following equations,

For ABCABC arrangement,

$$\begin{cases} \lambda_{\text{m1}} \geq 2\cdot\tau_{\text{m}} = \left(2-\dfrac{1}{3}\right)\cdot\tau_{\text{s}} \\ \lambda_{\text{m2}} \geq \lambda_{\text{m1}} + 4\cdot\tau_{\text{m}} \end{cases} \tag{23}$$

For AABBCC arrangement,

$$\begin{cases} \lambda_{\text{m1}} \geq \lambda_{\text{m2}} + 2\cdot\tau_{\text{m}} \\ \lambda_{\text{m2}} \geq 2\cdot\tau_{\text{m}} = \left(2-\dfrac{1}{3}\right)\cdot\tau_{\text{s}} \end{cases} \tag{24}$$

Meanwhile, λ_{m1} and λ_{m2} should also satisfy (7) and (8), and the final value of these two parameters are shown in TABLE II.

In consideration of the difficulty of mechanical installation of prototype, the air gap length of the machine is set as 1mm. Based on the previous work [22], the optimal ratio of the DC to total copper loss, k_{DC} is achieved around 0.3, when copper loss of DC to AC reaches 1:2. This is because DC windings are wound on the yoke of the module, which makes both sides of the coil functional, and therefore the magnetic and electrical load are equally distributed for maximum output force. Other parameters, such as split ratio k_{sp}, copper loss P_{loss}, are based on empirical values.

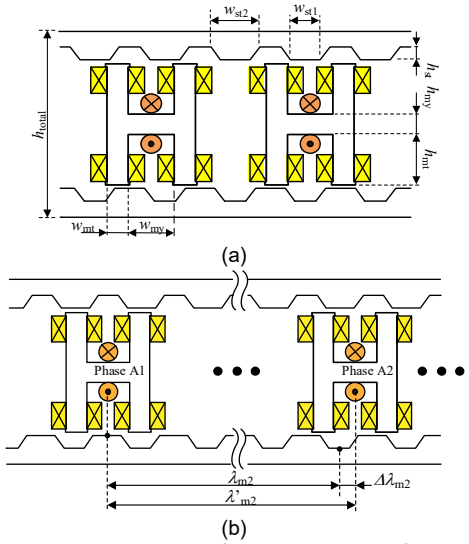

Fig.5. Geometric parameters of the proposed DS- MVRLM. (a) Dimension parameters of machine. *(b) Definitions of* λ_{m1}, λ_{m2}, $\Delta\lambda_{m2}$.

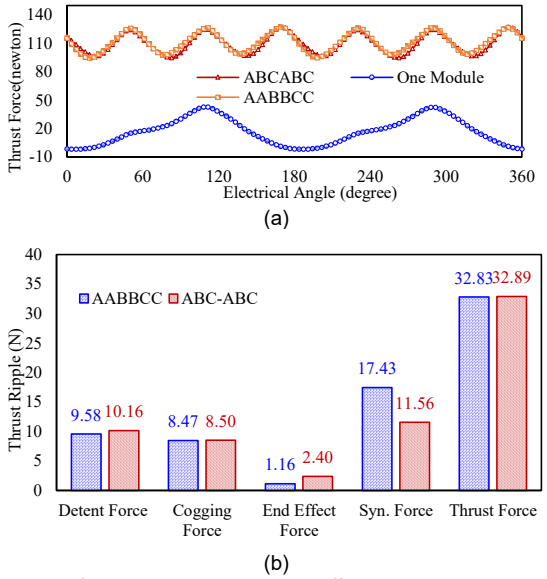

Fig.6. Thrust force characteristics with different module arrangements (a) Waveform of thrust force. (b) Ripple components of thrust force.

Two feasible module arrangements (ABCABC and AABBCC) can be applied to the proposed machine structure, which has different effect on the different components of the thrust force. In specific, as the detent force is caused by the interaction force between mover teeth and stator salient teeth, the detent force of the proposed machine varies according to different arrangement of the module. In comparison, since the interactions between different modules have been weakened by modularized design, the amplitude and phase of the main flux cannot be influenced by the arrangement of the module. Thereafter, the arrangement has little effect on the electromagnetic force.

TABLE II INITIAL DESIGN PARAMETERS OF DS-DC-MVRLM

Parameter	AABBCCABCABC	Parameter	AABBCCABCABC
τ_s, (mm)	τ_m*12/10	τ_m, (mm)	32.5
λ_{m1} (mm)	(4-1/3) τ_s (2-1/3) τ_s	λ_{m2} (mm)	$2\tau_s$ $5\tau_s$
L_m, (mm)	$11\tau_s$ | $10\tau_s$	L_{stk}, (mm)	50
P_{loss}, (W)	180	k_{DC},	0.3
h_{total}, t (mm)	80	k_{sp},	0.65
g, (mm)	1		

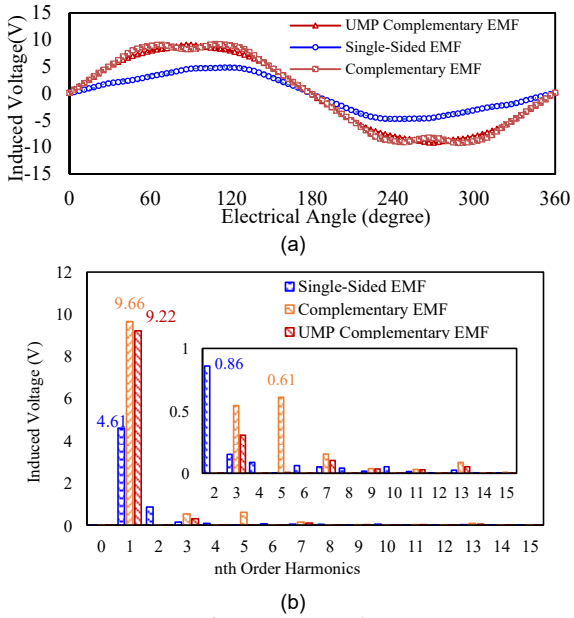

Fig.7. Induced voltage of machine with/ without UMP design. (a) Waveforms. (b) Spectrum of flux density distribution

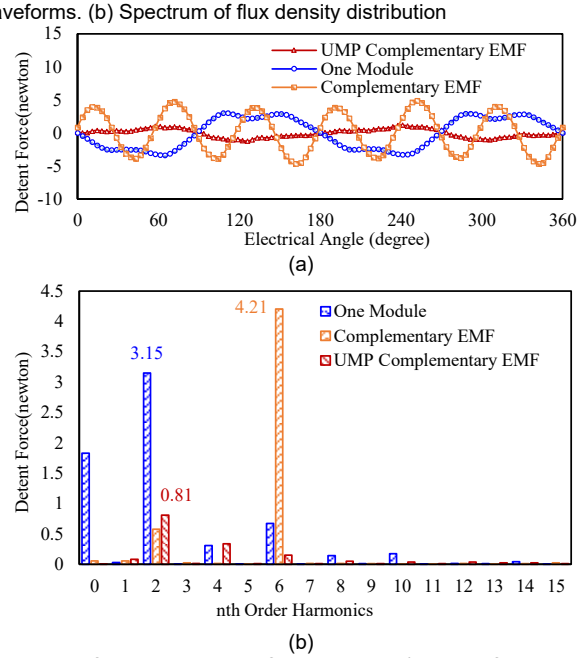

Fig.8.Detent force distribution of machine with/ without fractional pole-pair design. *(a) Waveform comparison. (b) Spectrum.*

Fig. 6 compares the different output thrust force of the machine with two arrangements, where Fig. 6(a) illustrates the waveforms of their output thrusts and Fig. 6(b) calculated the ripple composition of each force component. According to the results, thanks to the flux barrier of modular linear machine, the output on- load thrust results of machine with "ABCABC" and "AABBCC" arrangements are basically the same, which is 111N, 110N for thrust force in average, and 32.89N and 32.83N for thrust ripple. To be noticed, the end force of the machine AABBCC is slightly lower than that of ABCABC since the

interval between modules are much larger. Fig. 7 presents the induced voltage comparison of them.

Fig. 8(a) demonstrates the detent force of DS-DC-MVRLM with different arrangements, and Fig. 8(b) depicts the spectrum of it. The blue line illustrates the detent force of one H- shaped module, in which second- order harmonics is dominated. The orange line depicts the detent force of the modular linear machine with complementary structure, whose dominated harmonic is sixth- order harmonics. However, after applying FP-UMA arrangement to the linear machine, the amplitude of sixth- order harmonics in detent force is greatly suppressed, which is demonstrated as the red line in Fig. 8.

IV. Machine Design Consideration

A. Key Parameter Analysis of DS- MVRLM

The coefficients, defined as (25)(26), which include DC loss split ratio k_{DC}, split ratio k_{sp}, etc, are investigated under fixed copper loss at 180W. DC loss split ratio k_{DC} represents the ratio of DC copper loss to total loss, and split ratio k_{sp} is defined as the height of the primary mover to total height of the machine.

$$k_{dc} = P_{loss\_dc} / P_{loss\_total} \tag{25}$$

$$k_{sp} = (2h_{mt} + h_{my}) / h_{total} \tag{26}$$

Other initial dimensions of the proposed motor are listed in TABLE. II. The initial design parameters are selected based on the empirical value. The average thrust force F_t and the ratio of thrust ripple R_r, defined as (27), are set as objective functions.

$$R_r = \frac{F_{t\_max} - F_{t\_min}}{F_t} \tag{27}$$

The mover length is set as a constant value (390mm), and τ_m is fixed to 32.5mm for fair comparison. Based on the different slot-pole combination (τ_m/τ_s), secondary pole-pitches τ_s are calculated as 39mm for 10/12 τ_m/τ_s, 35.4mm for 11/12 τ_m/τ_s, 30mm for 13/12 τ_m/τ_s, 27.8mm for 14/12 τ_m/τ_s. In the previous section, it has been proved that there is little difference between 'ABCABC' and 'AABBCC' arrangements with the same τ_m/τ_s. Therefore, to simplify analysis, only 'ABCABC' arrangement is investigated in the design consideration analysis.

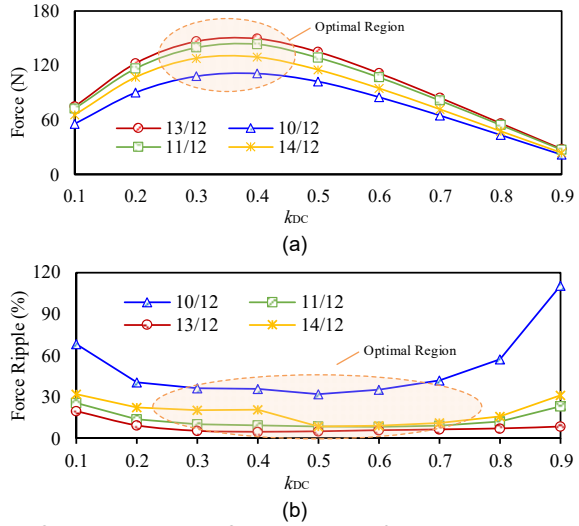

Fig.9. DC loss ratio to thrust force. *(a) Thrust force. (b) Force ripple.*

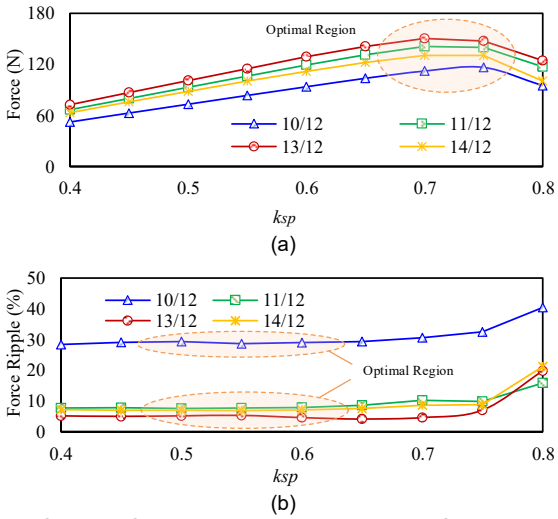

Fig.10. Influence of split ratio on the output thrust force. *(a) Average thrust force. (b) Force ripple ratio.*

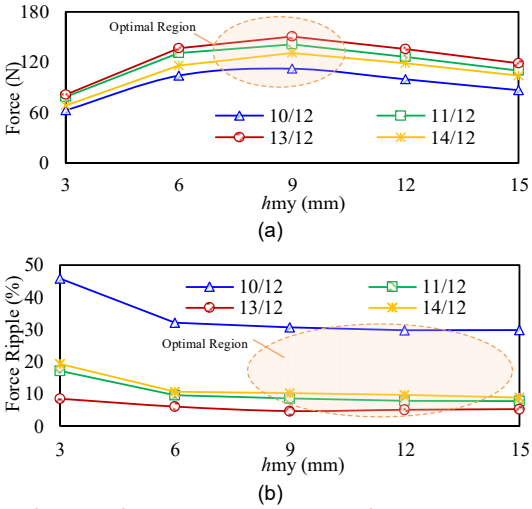

Fig.11. Influence of h_{my} on the output thrust force. *(a) Average thrust force. (b) Force ripple ratio.*

It is shown in Fig. 9 that when the optimal value of k_{dc} is around 0.33, the F_t reaches maximum (149.5N), in the machine with 13/12 τ_m/τ_s slot-pole combination. This is because DC windings are wound on the yoke of the module, making them functional in both of the half circles of the whole period, whose utilization ratio is higher than the armature windings. Therefore, when copper loss of DC to AC reaches 1:2, the magnetic and electrical load are equally distributed. On the other hand, it can be found that in Fig. 10, the optimal value for split ratio k_{sp} is around 0.7. Although higher k_{sp} provides larger space for DC and armature winding, when k_{sp} increases furtherly, the space for secondary is suppressed, and the output force deceased thereafter due to the saturation problem. Meanwhile, the force ripple greatly increases as well for the same reason.

Furthermore, the height of the primary yoke is investigated under fixed split ratio (0.7). Fig. 11(a) presents the influence of the primary yoke height on the average thrust force, while the impact of it on the thrust ripple ratio is presented in Fig. 11(b). It is found that the optimal value for h_{my} is around 9mm. The average thrust will be compromised due to the saturation issue when the value of h_{my} is too small. However, when h_{my} is overlarge, the space for field and armature winding is suppressed, which limits the output thrust force.

B. Modified Mover Pole- Pitch λ'_{m2}.

The mover pole-pitch coefficient, denoted as k_λ, is defined as the ratio between $\Delta\lambda_{m2}$ and τ_s, which is expressed as (28).

$$k_\lambda = \Delta\lambda_{m2} / \tau_s \tag{28}$$

Fig. 12 presents the influence of k_λ. It can be found that when k_λ=0, the thrust force achieves highest in average, reaching 150.5N. However, the output thrust force fluctuates largely, especially in the design of 10/12 τ_m/τ_s slot-pole combination. As shown in Fig. 12, regardless of the slot pole combination, the optimized value of k_λ is around ±0.1 to achieve the lowest thrust ripple which is closed to the condition in (16) for electro-magnetic force suppression. This can be attributed to the large proportion of electromagnetic force in the total thrust force of the motor, which has been proved in the previous section.

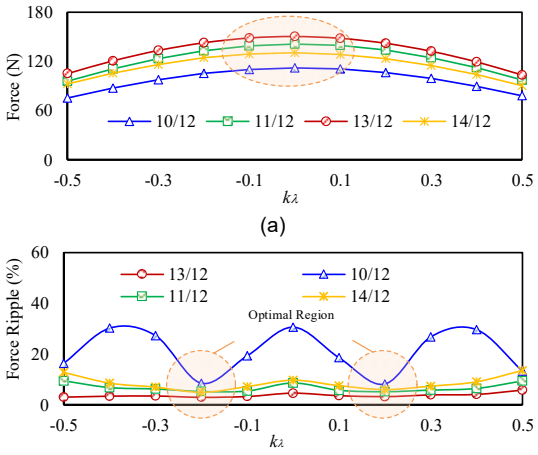

Fig.12. Influence of k_λ on the output thrust force. (a) Average thrust force. (b) Force ripple ratio.

C. Sensitivity Analysis of Parameters and Optimized Design Parameters

To analyze the significance of the above parameters, the sensitivity of parameters at initial value $S_{oj}(x_i)$ is defined as follows,

$$S_{oj}(x_i) = \frac{\Delta O_j}{O_j(x_{i0})} / \frac{\Delta x_i}{x_{i0}} = \frac{x_{i0}}{O_j(x_{i0})} \cdot \frac{\partial O_j}{\partial x_i}\bigg|_{x_i = x_{i0}} \tag{29}$$

where O_j is the objective function, such as average thrust force or force ripple ratio of the machine, ΔO_j is the variation value of objective function, x_i is the initial value of the optimal parameter, and Δx_i is the variation value of the optimal parameters. Taken machine with τ_m/τ_s=10/12 as an example, TABLE III presents the optimal range and sensitivity of the parameters, where S_{o1} represents the sensitivity of output thrust and S_{o2} represents that of the force ripple. According to TABLE III, split ratio k_{sp} is one of the most significant parameters to thrust force and force ripple of the machine. DC ratio k_{DC} basically has no impact on the thrust ripple of the machine. It can be found that the sensitivity of k_λ to thrust ripple has reached 0.57, which indicates that it is much more significant to force ripple than average force. Based on the previous design analysis, the optimal design parameters of four feasible slot pole combinations and their performances are listed in TABLE IV. Comparing with other slot/pole combinations, τ_m/τ_s=13/12 design achieves highest output thrust under the same copper loss (180W). Meanwhile, regardless of the geometric dimensions of the motor, τ_m/τ_s=13/12 design could obtain lowest detent force along with thrust ripple compared with that of other feasible slot/ pole combinations.

TABLE III SENSITIVITY ANALYSIS OF DC-MVRLM

Symbol	Parameter	unit	Initial	Range	$S_{o1}(x_i)$	$S_{o2}(x_i)$
k_{sp}	*Split ratio*	-	0.3	[0.2, 0.5]	0.81	0.72
k_{dc}	*Ratio of DC to total loss*	-	0.3	[0.1, 0.9]	0.13	-0.086
h_{my}	*Height of mover yoke*	mm	10	[6, 14]	0.48	-0.47
k_λ	*Mover pole-pitch coefficient*	-	0	[-0.5, 0.5]	-0.031	-0.57

TABLE IV OPTIMAL DESIGN PARAMETERS OF DC-MVRLM

Parameter	10/12	11/12	**13/12**	14/12
L_m, Mover teeth length (mm)		390		
τ_s, Stator pole pitch (mm)	39	35.4	**30**	27.8
$\Delta\lambda_m$, Mover pole pitch offset (mm)	3.9	3.5	**2.9**	2.8
w_{mt}, Width of mover teeth (mm)	8.7	9.0	**9.1**	8.7
h_{my}, Height of mover yoke (mm)	9.0	9.0	**9.1**	9.2
h_{mt}, Height of mover teeth (mm)	19.2	20.7	**18.5**	14.3
h_{sy}, Stator yoke height (mm)	7.4	7.0	**7.1**	6.3
k_{sp}, Split ratio	0.70	0.69	**0.68**	0.71
k_{dc}, DC to total loss ratio	0.36	0.34	**0.34**	0.36
N_{ac}, Number of AC windings	70	68	**60**	64
N_{dc}, Number of DC windings	145	141	**123**	148
P_{loss}, Copper loss (W)		180		
F_t, Rated thrust force (N)	91.51	115.9	**121.3**	109.00
R_r, Force ripple ratio (%)	6.9	5.0	**2.3**	4.4

V. PERFORMANCE EVALUATION

A. Open-Circuit Performance of DS- MVRLM

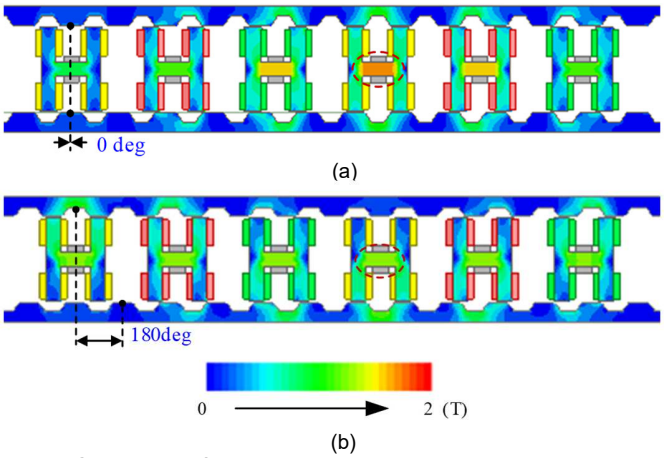

Fig.13 Open-circuit flux density distributions. *(a) MVRLM without complementary structure. (b) MVRLM with complementary structure.*

Based on the design parameters of the machine with 13/12 τ_m/τ_s, the flux distributions of the with complementary and uncomplimentary design are plotted in Fig.13. It is shown in the red dash circle that due to the double-sided complementary design, the saturation issue in the yoke of the machine has been relieved. Fig.14 presents induced voltage under open- circuit condition of MVRLM with/ without complementary structure. Meanwhile, the machine with/without FP-UMA machine is also compared. The results indicate that the complementary structure boosts the fundamental harmonic of induced voltage, and thanks to FP-UMA design, the 5th order and 7th order harmonics of induced voltage have been reduced, indicating that 6th order harmonic in the electromagnetic force will be eliminated. Comparing with the machine without complementary structure, the total harmonics distortion (THD) has been reduced from 5.65% to 1.13%, and further to 0.85% after FP-UMA is adopted.

B. Thrust Characteristics

Fig. 15 compares the thrust force characteristics of the machine with/ without UMP design. The machines are

controlled with field-oriented control (FOC) method. According to Fig. 15, after applying the proposed UMP design, the ripple of output thrust force has been reduced from 4.18 N to 2.75N under fixed copper loss (P_{loss}=180W), and the detent force is also suppressed evidently. Fig. 16 summarized the force ripple components of the machine. It can be found that UMP design could greatly suppress the synchronous force ripple as it reduces the higher order harmonics in the induced voltage.

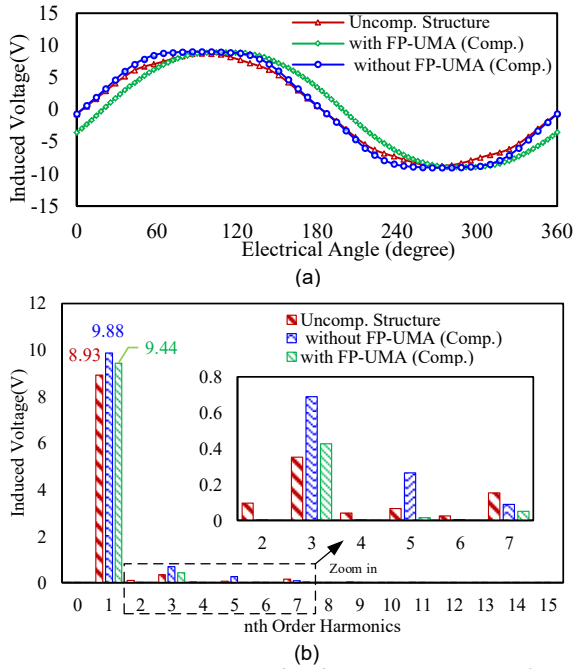

Fig.14. The Induced voltage of DC-MVRLM. *(a) waveforms. (b) Spectrums.*

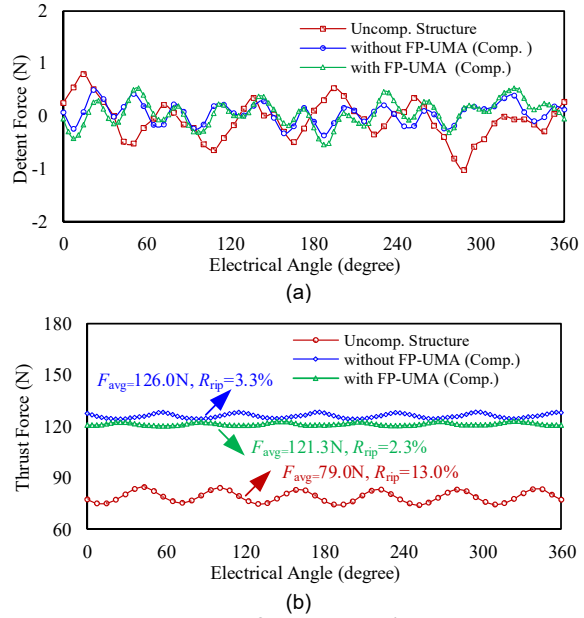

Fig.15. Thrust characteristics of machine with/ without FP-UMA design. *(a) Detent force. (b) Total thrust force.*

Fig.16 presents the average thrust of machine with/ without complementary structure and proposed FP-UMA design under different electrical loads and the thrust ripple ratio R_{rip} of them are also presented as bar charts. The calculation results have shown that uncomplimentary structure will compromise the average thrust force of the machine because of easy saturation. Meanwhile, the force ripple of the machine is also large because of high-order harmonics in the induced voltage and detent force. In collocation with FP-UMA design, the force ripple of the machine is further suppressed, whose thrust ripple ratio R_{rip} can be reduced from 3.3% to 2.3% under rated copper loss(180W), and 4.6% to 2.2% under over-excited copper loss (450W). This also demonstrates that the proposed method has evident inhibitory effect on higher harmonics introduced by saturation. TABLE V has summarized the performance of the proposed motor with/without complementary structure and FP-UMA design under rated condition, including its force characteristics, efficiency, etc.

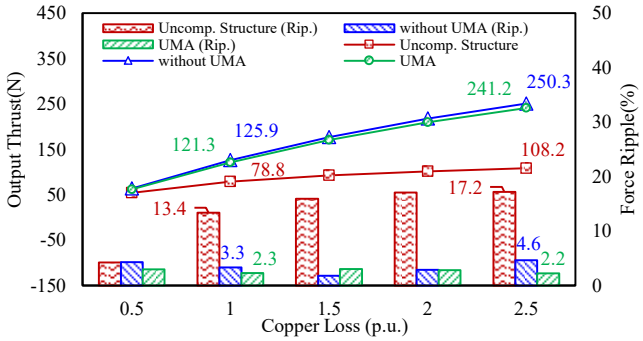

Fig.16. Thrust characteristics of DC-MVRLM under different loads.

TABLE V PERFORMANCES OF MACHINES WITH/ WITHOUT FP-UMA DESIGN

	Uncomp. Structure	without FP-UMA	FP-UMA
Pole Pair Number of Stator	13	13	13.2
Mover Length, L_m (mm)	390	390	395.8
Stack Length, L_{stk} (mm)		50	
Air gap Length, g (mm)		1	
Current Density, J_e (A/mm^2)		5.98	
Turns of AC, N_{ac}		60	
Turns of DC, N_{dc}		123	
DC resistance, R_{dc} (ohm)		2.11	
Phase Resistance, R_{ac} (ohm)		1.37	
Rated Speed, v (m/s)		10	
Thrust force (N)	78.8	126.0	121.3
Thrust ripple ratio, R_{rip} (%)	13.4	3.3	2.3
Power factor, pf	0.30	0.34	0.34
Copper loss, p_{cu} (W)		180	
Iron loss, p_{fe} (W)	30.83	35.76	35.76
Efficiency, η (%)	78.80	85.34	85.00

C. Loss, and Efficiency

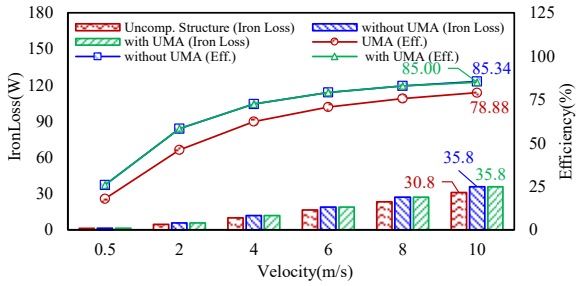

Fig.17. Loss and efficiency characteristics of DC-MVRLM under different operation speed.

Loss and efficiency are essential indicators to reflect the power consumption of the motor. After applying FP-UMA design to the motor, the harmonics in the air gap have been changed, which may affect core loss and efficiency of the motor inevitably. The iron loss of the motor can be calculated as following equation [23],

$$P_{Fe}=P_h+P_e+P_c=K_h f_e B_m^2+K_e(f_e B_m)^{1.5}+K_c(f_e B_m)^2 \quad (30)$$

where K_h is the hysteresis core loss coefficient, K_c is eddy effect coefficient, K_e is the excess coefficient, f_e is the electrical frequency, and B_m is the flux density in the core. According to (30), the iron loss is varied under different operation velocity.

Fig.17 presents the iron loss and efficiency of the linear motor at speed of 0.5 m/s to 10m/s. The results revealed that considering its direct-drive application, the iron loss of the motor is relatively low comparing with the iron loss (from 2.4W to 68.5W). The bar charts show that the iron loss of motors with/ without FP-UMA design share basically the same iron loss. Accordingly, the proposed FP-UMA design has little impact on the iron loss of the motor. In terms of efficiency, there is little difference between machines with/ without FP-UMA design, indicating that the proposed FP-UMA method with fractional pole-pair design has limited effect on the efficiency of the machine.

VI. Experimental Verification

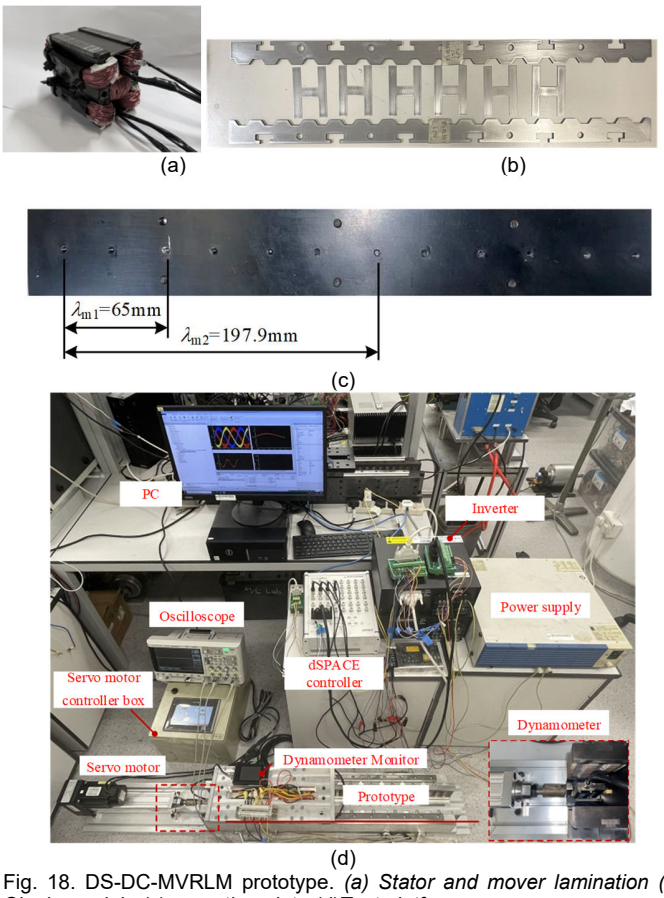

Fig. 18. DS-DC-MVRLM prototype. *(a) Stator and mover lamination (b) Single module (c) mounting plate (d)Test platform*

Based on the geometric parameters listed in TABLE. VI, the prototype is manufactured to verify the feasibility of the proposed design. DW540_50 is selected as the laminated iron material, whose saturation point is 1.8T. AWG 22 is selected for the copper wire. The laminations of both stator and the modular movers are shown in Fig.18 (a). Fig. 18 (b) shows the assembly of sole module of the mover. The concentrated windings are adopted to simplify the winding process and boost the filling factor as well. Fig. 18 (c) demonstrates the mounting plate for the modular mover. The FP-UMA design is applied to the motor via unequally distributed locating hole, whose λ_{m2} is designed as 197.9mm. Fig. 18 (d) demonstrates the experiment platform for the prototype, including servo motor for induced voltage test and dSPACE controller and inverter for on-load test. In addition, oscilloscope and dynamometer is utilized to read the induced voltage and thrust force of the prototype respectively.

In the open- circuit experiment, the prototype excited by i_{dc}=1A, 3A and 6A is driven by servo motor at speed of 1m/s, and the induced voltage results are presented in Fig. 19. The amplitude of three-phase EMF of simulated result is 1.51V, 4.62V and 9.27V respectively. And the measured value is 1.45V, 4.51V and 9.10V respectively. The errors between FEA and test are 4%, 2.5% and 2% respectively, which is mainly caused by the end effect and measurement error. The simulation value is well consistent with the experimental result. Fig. 20(a) presents the static on-load test results of the machine under different power angles, when DC excitation currents and RMS value of AC excitation currents are set as 1A, 3A and 6A respectively, and the prototypes are kept still when DC and AC excitations are applied to the prototype. Fig. 20(b) measures the thrust force of the machine under different excitation currents. The measured results agree well with FEA results. The errors of them are mainly caused by the limitation of the dynamic performance of dynamometer.

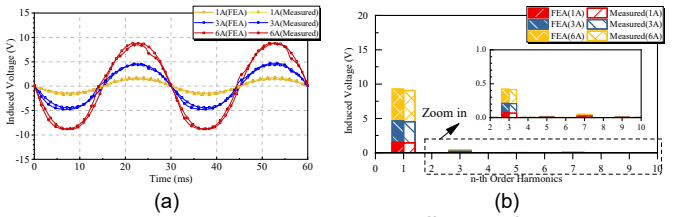

Fig. 19. Measured induced voltage under different DC excitations. *(a) Waveforms. (b) Spectrum.*

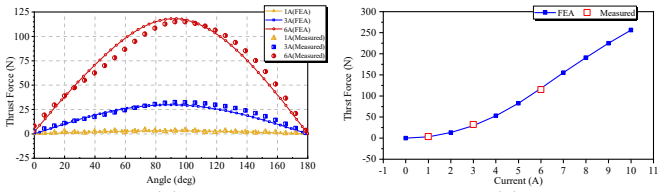

Fig. 20. Static thrust force characteristic with different excitations. *(a) Power angle characteristic. (b) thrust force of different current excitations.*

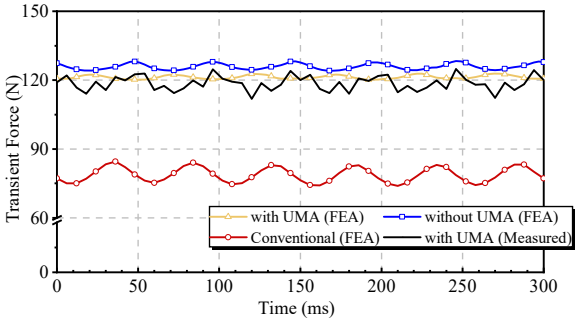

Fig. 21 Transient thrust force characteristic with different configurations.

The dynamic test of the machine is conducted via primary field-oriented control (FOC). Fig. 21 presents the dynamic test of prototype and the machine with conventional structure using FOC algorithm, and the speed of the mover keeps 0.1m/s, where the black line indicates the measured thrust force of the prototype, the yellow line indicates the thrust force of the prototype calculated by FEA, the blue line indicates the machine with complementary structure but without UMA design, and the red line indicates the machine without complementary structure. The RMS value of the phase current is 6A, and DC current in the field winding is set as 6A.

It is shown that the thrust force of the machine in average is tested as 118.58N, which is slightly lower than that of the FEA

calculation due to the transverse end effect. It is also tested that the thrust ripple of the machine is approximately 11%. This is mainly caused by measuring error of dynamometer, installation accuracy and workmanship of the prototype. FEA indicates the output force of the machine under ideal condition. It is shown that the complementary structure could greatly boost the thrust force of the machine and reduce the thrust ripple of it, and the proposed UMA method could further smooth the thrust ripple of the machine.

VII. Conclusion

In this paper, a double- sided modularized variable reluctance linear machine is proposed, and a fractional pole pair unequal module arrangement method for it has been investigated. Both FEA and test results have shown that the newly proposed method could effectively reduce the thrust ripple of the machine. In specific, some conclusions can be drawn as follows.

1) By adopting complementary structure, the double-sided MVRLM could boost the output thrust of the machine by 59.8%, and the force ripple ratio of the machine is also suppressed from 13.3% to 3.3% under rated power (180W). 2) Proposed FP-UMA design could effectively suppress the higher-order harmonics in induced voltage as well as detent force by modifying the distance of modules within one phase λ_{m2}. For the machine with 13/12 τ_m/τ_s, when $\lambda'_{m2}=6.6\tau_s$, and the pole-pair number of the machine is modified from 13 to 13.2, the thrust ripple ratio of the machine can be reduced from 3.3% to 2.3% at machine's rated condition (P_{loss}=180W), and 4.6% to 2.2% (P_{loss}=450W) at over-loaded condition, indicating that the proposed method is also suitable for over-loaded condition.

Due to the limitation of power supply in the lab, the rated power of the prototype is designed to be relatively lower than that of the practical use. However, the proposed method suppressing thrust ripple is effective in all kinds of power level, which makes it can be easily applied in RTS system.

Acknowledgments

This work was supported by the National Natural Science Foundation of China under Project 52077187 and in part by the Research Grant Council of the Hong Kong Government under Project PolyU 152143/18E and PolyU 152109/20E.

References

[1] A. A. Faiad and I. Gowaid, "Linear generator technologies for wave energy conversion applications: A review," in 2018 53rd International Universities Power Engineering Conference (UPEC), 2018, pp. 1-6: IEEE.

[2] I. Boldea, L. N. Tutelea, W. Xu, and M. Pucci, "Linear Electric Machines, Drives, and MAGLEVs: An Overview," IEEE Transactions on Industrial Electronics, vol. 65, no. 9, pp. 7504-7515, 2018.

[3] Y. Du and N. Jin, "Research on characteristics of single-sided linear induction motors for urban transit," in 2009 International Conference on Electrical Machines and Systems, 2009, pp. 1-4: IEEE.

[4] J. Pan, Y. Zou, and G. Cao, "An asymmetric linear switched reluctance motor," IEEE Transactions on Energy conversion, vol. 28, no. 2, pp. 444-451, 2013.

[5] Z. Li, X. Zhao, S. Niu, and W. Fu, "Analysis and Design of a New Relieving-DC-Saturation Transverse-Flux Tubular Motor with Complementary Magnetic Circuit," IEEE Transactions on Magnetics, vol. 57, no. 6, pp. 1-5, 2021.

[6] L. Wenlong, K. T. Chau, L. Chunhua, and Q. Chun, "Design and Analysis of a Flux-Controllable Linear Variable Reluctance Machine," IEEE Transactions on Applied Superconductivity, vol. 24, no. 3, pp. 1-4, 2014.

[7] T. W. Ching, Y. Shi, W. Li, and L. Jian, "Design and Analysis of a Magnetless Linear Variable Reluctance Motor with Modular Mover Units for Electric Propulsion," IEEE Transactions on Applied Superconductivity, vol. 30, no. 4, pp. 1-5, 2020.

[8] W. Hao and Y. Wang, "Comparison of the stator step skewed structures for cogging force reduction of linear flux switching permanent magnet machines," Energies, vol. 11, no. 8, p. 2172, 2018.

[9] J. H. Kim, Y. Li, E. Cetin, and B. Sarlioglu, "Influence of rotor tooth shaping on cogging torque of axial flux-switching permanent magnet machine," IEEE Transactions on Industry Applications, vol. 55, no. 2, pp. 1290-1298, 2018.

[10] Z. Yu-wu, L. Sang-Gun, C. Koon-Seok, and C. Yun-Hyun, "Investigation of Auxiliary Poles Design Criteria on Reduction of End Effect of Detent Force for PMLSM," IEEE Transactions on Magnetics, vol. 45, no. 6, pp. 2863-2866, 2009.

[11] C.-T. Liu, C.-C. Hwang, P.-L. Li, S.-S. Hung, and P. Wendling, "Design Optimization of a Double-Sided Hybrid Excited Linear Flux Switching PM Motor With Low Force Ripple," IEEE Transactions on Magnetics, vol. 50, no. 11, pp. 1-4, 2014.

[12] I. Eguren, G. Almandoz, A. Egea, S. Zarate, and A. Urdangarin, "Thrust Ripple Reduction in Linear Switched-Flux Machines via Additional Pole Optimisation," IEEE Transactions on Energy Conversion, pp. 1-1, 2022.

[13] C. Zhang et al., "A Low Detent Force DS-PMSLM Based on the Modulation of Cogging and End Forces," IEEE Transactions on Industrial Electronics, vol. 70, no. 1, pp. 721-730, 2023.

[14] S. L. Ho, Q. Wang, S. Niu, and W. Fu, "A novel magnetic-geared tubular linear machine with Halbach permanent-magnet arrays for tidal energy conversion," IEEE Transactions on Magnetics, vol. 51, no. 11, pp. 1-4, 2015.

[15] J. Wang and D. Howe, "Tubular modular permanent-magnet machines equipped with quasi-Halbach magnetized magnets-part I: magnetic field distribution, EMF, and thrust force," IEEE Transactions on Magnetics, vol. 41, no. 9, pp. 2470-2478, 2005.

[16] X. Sun, M. Wu, C. Yin, and S. Wang, "Model Predictive Thrust Force Control for Linear Motor Actuator used in Active Suspension," IEEE Transactions on Energy Conversion, vol. 36, no. 4, pp. 3063-3072, 2021.

[17] Y. Gao, R. Qu, D. Li, and F. Chen, "Force Ripple Minimization of a Linear Vernier Permanent Magnet Machine for Direct-Drive Servo Applications," IEEE Transactions on Magnetics, vol. 53, no. 6, pp. 1-5, 2017.

[18] X. Huang, Z. Qian, Q. Tan, J. Li, and B. Zhou, "Suppressing the Thrust Ripple of the Permanent Magnet Linear Synchronous Motors With Different Pole Structures by Setting the Modular Primary Structures Differently," IEEE Transactions on Energy Conversion, vol. 33, no. 4, pp. 1815-1824, 2018.

[19] [10] C. Shi, R. Qu, D. Li, X. Ren, Y. Gao, and Z. Chen, "Analysis of the Fractional Pole-Pair Linear PM Vernier Machine for Force Ripple Reduction," IEEE Transactions on Industrial Electronics, vol. 68, no. 6, pp. 4748-4759, 2021.

[20] Q. Tan, M. Wang, L. Li, and J. Li, "Research on Noninteger Pole Number for Segmental Permanent Magnet Linear Synchronous Motor," IEEE Transactions on Industrial Electronics, vol. 68, no. 5, pp. 4120-4130, 2020.

[21] R. Cao, M. Cheng, and W. Hua, "Investigation and General Design Principle of a New Series of Complementary and Modular Linear FSPM Motors," IEEE Transactions on Industrial Electronics, vol. 60, no. 12, pp. 5436-5446, 2013.

[22] X. Zhao and S. Niu, "Development of a novel transverse flux tubular linear machine with parallel and complementary PM magnetic circuit for precision industrial processing," IEEE Transactions on Industrial Electronics, vol. 66, no. 6, pp. 4945-4955, 2018.

[23] J. Wang, T. Ibrahim, and D. Howe, "Prediction and Measurement of Iron Loss in a Short-Stroke, Single-Phase, Tubular Permanent Magnet Machine," IEEE Transactions on Magnetics, vol. 46, no. 6, pp. 1315-1318, 2010.